Supplementary Information

Coupling anodic/cathodic energy storage through *in-situ* heterostructure regulation of ordered microporous carbon for sodium-ion hybrid capacitors

Juan Li,[a,b] Bo Wang,[c] Tianzhao Hu,[b,d] Yuzuo Wang,[b,e,f] Zhenhua Sun,[b] Chunzhong Wang,[a] Dong Zhang,[a,*] Zhuopeng Wang,[c,*] Feng Li[b,*]

[a] Key Laboratory of Physics and Technology for Advanced Batteries (Ministry of Education), College of Physics, Jilin University, Changchun 130012, China.

[b] Shenyang National Laboratory for Materials Science, Institute of Metal Research, Chinese Academy of Sciences, Shenyang 110016, China.

[c] Department of Chemistry, College of Sciences, Northeastern University, Shenyang 110819, Liaoning, China.

[d] School of Materials Science and Engineering, Zhengzhou University, Zhengzhou 450001, China.

[e] Ningbo CRRC New Energy Technology Co. Ltd, 552 Wuxiang West Road, Ningbo 315112, China.

[f] State Key Laboratory of Chemical Engineering, School of Chemical Engineering and Technology, Tianjin University, Tianjin 300350, China.

*E-mail: fli@imr.ac.cn; dongzhang@jlu.edu.cn; wangzhuopeng@mail.neu.edu.cn

Experimental

Chemicals:

Furfuryl alcohol ($C_5H_6O_2$ ≥98.5%), mesitylene (C_9H_{12} ≥99.5%), hydrochloric acid (HCl 37%), and hydrogen fluoride (HF) were purchased from Sinopharm Chemical Reagent Co., Ltd. Zeolite Y powder (NaY CBV100) was obtained from Zeolyst International Company. XFP06 activated carbon was provided by Nanjing XFNANO Materials Tech Co., Ltd. YP-50F activated carbon was produced by Kuraray Co., Ltd. Hard carbon was purchased from Guangdong Canrd New Energy Technology Co., Ltd. All the chemical reagents in the paper were used without further purification.

Preparation of Ordered Microporous Carbon (OMC)

The materials were prepared according to reference.[1, 2] In typical process, the commercial NaY zeolite (5 g) was calcinated at 530 °C for 4 hours in muffle furnace, vacuumed for another 4 hours at 150 °C to further evacuate the microporous channels. 50 ml of furfuryl alcohol (FA) was selected to impregnate into the pretreatment NaY zeolite at room temperature under vacuum condition. The obtained sample was stirred overnight with nitrogen atmosphere, and filtered, and washed off with mesitylene for three times. The powder was heated in oil bath at 80 °C for 24 hours under nitrogen flow, and then heated to 150 °C for 8 hours to polymerize FA in NaY zeolite. The obtained dark gray powder was denoted as PFA@NaY.

2 g of PFA@NaY powder was placed in tubular quartz reactor. After heating to 700 °C in nitrogen atmosphere, 2% propylene diluted by nitrogen with total gas flow of 200

$ml \cdot min^{-1} \cdot g^{-1}$ was passed through the reactor for 4 hours to conduct chemical vapor deposition of carbon into NaY zeolite. The temperature of the reactor was raised to 900 °C for 3 hours to ensure that the polymers in the micropores were fully carbonized. The obtained complex was denoted as PFA/C@NaY. Finally, about 500 mg of OMC sample was obtained after removal of NaY template by HF and HCl treatment.

Preparation of Nitrogen-doped Ordered Microporous Carbon (N-OMC)

2 g of PFA@NaY powder was placed in tubular quartz reactor. After heating to 700 °C in nitrogen atmosphere, 2% propylene diluted by nitrogen with total gas flow of 100 $ml \cdot min^{-1} \cdot g^{-1}$ was passed through the reactor for 2 hours to conduct chemical vapor deposition of carbon into NaY zeolite. The temperature was raised to 800 °C at a heating rate of 5 $°C \cdot min^{-1}$ under nitrogen flow. When the temperature reached the predetermined temperature, the acetonitrile vapor was introduced into the reactor through bubbler at N_2 flow rate of 100 $ml \cdot min^{-1} \cdot g^{-1}$ for 30 min, and the bubbler temperature was maintained at 0 °C through ice bath. At last, the temperature of the reactor was raised to 900 °C for 1 hour to ensure that the polymers in the micropores were fully carbonized. The obtained complex was denoted as PFA/NC@NaY. About 500 mg of N-OMC sample was obtained after removal of NaY template by HF and HCl treatment.

Structural characterizations

X-ray diffraction (XRD) analysis was obtained on Rigaku D/max 2500 diffractometer equipped with Cu Kα radiation (λ=1.5418 Å). The morphology and structure of the materials were characterized using SEM (FEI Nova NanoSEM 430) and TEM (Tecnai

F20). Energy dispersive X-ray spectroscopy (EDS) elemental maps was performed on FEI Tecnai F20 microscope equipped with an Oxford EDS analysis system. Raman spectra were recorded on Horida LabRAM HR800 laser Raman spectrometer using a laser excitation of 633 nm. N_2 adsorption-desorption isotherms were measured at 77 K using Micromeritics ASAP2020. The specific surface area was calculated using the Brunauer-Emmett-Teller (BET) method. The pore size distribution was determined based on Density Functional Theory (DFT) method. X-ray photoelectron spectroscopy (XPS) measurements were carried out by ESCALAB 250 instrument with Al Kα radiation.

Electrochemical Measurements

Electrochemical performances were measured via coin cells assembled inside Ar-filled glovebox. The working electrodes were prepared by mixing the active materials (OMC, N-OMC, hard carbon, YP-50F, XFP06, 80 wt%), conductive agent (Ketjenblack, 10 wt%), and binder (Polytetrafluoroethylene, 10 wt%) in mortar with ethanol to form gummy-like mixture, and rolling into a uniformly thin film which was cut into disks of 10 mm in diameter. The disks were dried under vacuum to remove solvent, and pressed onto stainless steel mesh to produce the working electrode. The mass loading of electrodes was about 1.2-1.9 $mg \cdot cm^{-2}$. The electrolyte was composed of 1 M $NaClO_4$ in the 1:1 (v/v) mixture of ethylene carbonate (EC) and propylene carbonate (PC) with the additive of 5 % fluoroethylene carbonate (FEC). The half-cell was assembled by Na-metal foil as counter and reference electrode in 2032-type coin cells. When the

OMC, hard carbon or N-OMC materials as anode were tested, the electrodes were pre-activated at low current density (0.1 $A \cdot g^{-1}$). Whatman glass microfiber (GF/C) was used as the separator. The full-cell was assembled with OMC as anode and N-OMC as cathode (= 1:2.5 ratio for weights) in 2025-type coin cells. The mass ratio of anode to cathode was obtained based on the specific capacities of two electrodes with current density of 0.1 $A \cdot g^{-1}$, and was used to balance the capacity of each electrode. Before assembling full-cell, the OMC anode was pre-activated for 5 cycles at 0.1 $A \cdot g^{-1}$ in a Na||OMC half-cell and then discharged to cut-off voltage of 0.1 V (vs. Na/Na^+). In order to compare the performance of self-discharge, the symmetric electrochemical capacitors with commercial activated carbon (YP-50F or XPF06) as working electrodes were also assembled and tested, denoted as YP-50F||YP-50F or XPF06||XPF06.

Galvanostatic charge/discharge, cycling stability and rate capability were measured using Landian multichannel battery tester. Cyclic voltammetry and electrochemical impedance spectra (EIS, 10 mHz-200 KHz) were carried out using VSP-300 multichannel workstation. The galvanostatic intermittent titration technique (GITT) measurement in the potential range of 0.01-3.0 V (vs. Na/Na^+) was programmed by providing a constant current density of 0.1 $A \cdot g^{-1}$ for 5 min, followed by open circuit relaxation for 20 min. The energy density (E) and power density (P) of the assembled sodium-ion hybrid capacitors were calculated according to the equations:[3, 4]

$$E = \frac{V_{max} + V_{min}}{2} \cdot \frac{I \times t}{m} \cdot \frac{1}{3.6}$$

$$P = \frac{E \times 3600}{t}$$

where V_{min} and V_{max} are the initial and final voltage of discharge, respectively, I is the

discharge current, t is the discharge time, and m is the total mass of active materials in both electrodes.

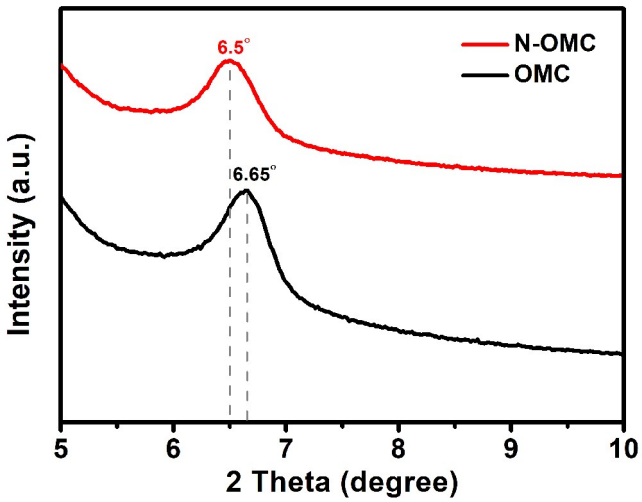

Fig.S1. The enlarged view of XRD patterns for OMC and N-OMC at small angles.

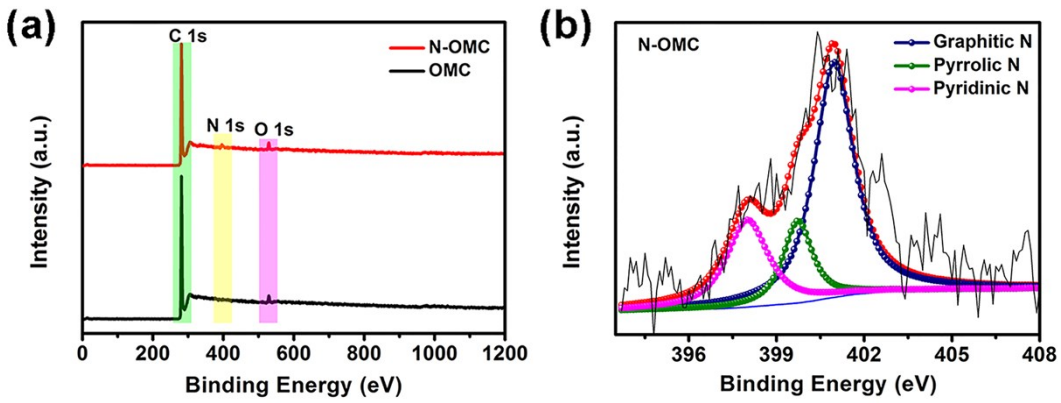

Fig.S2. (a) XPS spectra of OMC and N-OMC. (b) High-resolution N 1s XPS spectra of N-OMC.

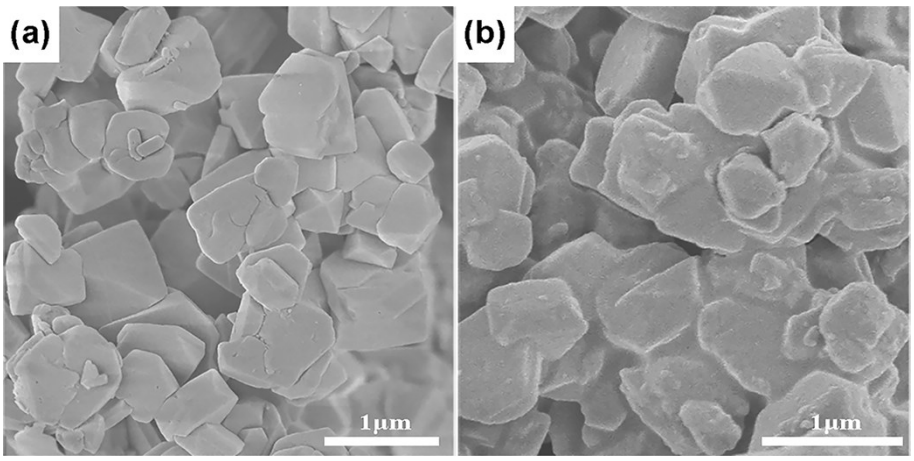

Fig.S3. SEM images of (a) NaY zeolite and (b) PFA@NaY.

The morphologies of NaY zeolite and PFA@NaY are characterized, shown in Fig. S3. The NaY zeolite and PFA@NaY both show irregular morphology. Compared with NaY zeolite, the PFA@NaY sample reveals similar shape and size in connection with the preparation route, except the coating layer of poly(furfuryl alcohol).

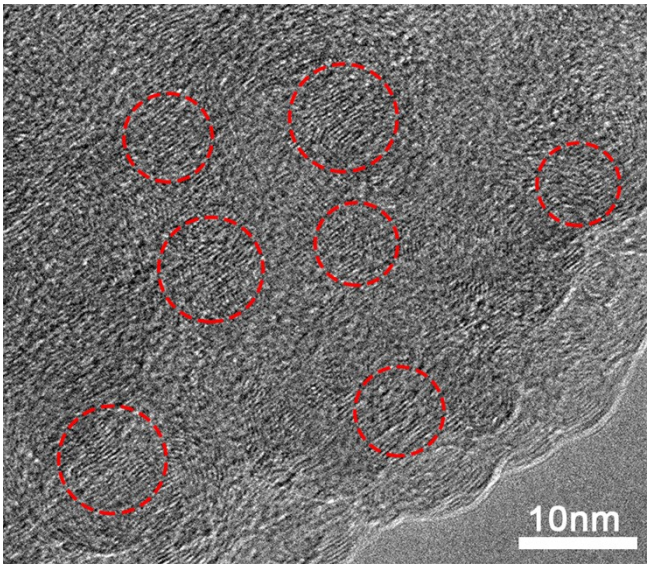

Fig.S4. HRTEM image of OMC.

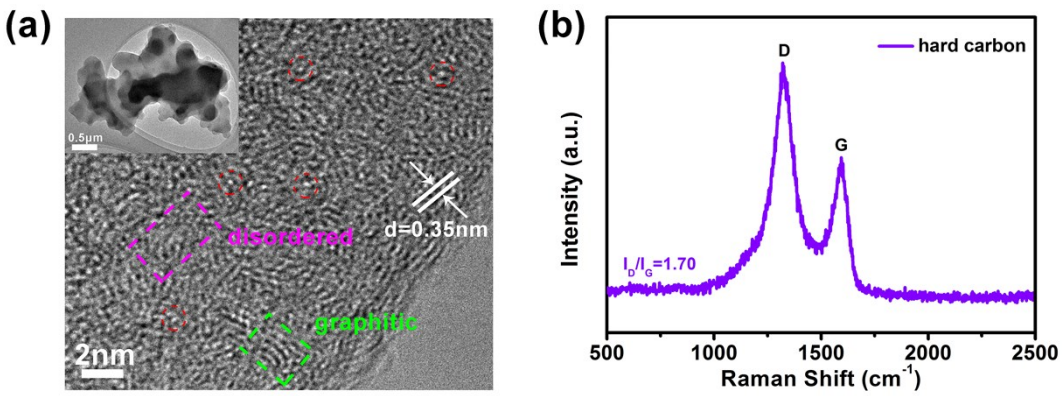

Fig.S5. (a) TEM and HRTEM images. (b) Raman spectra of hard carbon.

The hard carbon was characterized using TEM and Raman spectra, showed in Fig. S5. The irregular morphology displayed in inset of Fig. S5a is observed. The HRTEM image shows the highly disordered regions of carbon and some randomly graphitic domains. In addition, micropores exist in the material, and are circled in red. The interlayer spacing of hard carbon is around 0.35 nm, higher than that of graphite (0.335 nm). The characteristic bands (D- and G- band) are clearly observed, and corresponding intensity ratio (I_D/I_G) is 1.70. Compared with OMC (I_D/I_G = 0.765), hard carbon has higher disorder of carbon.

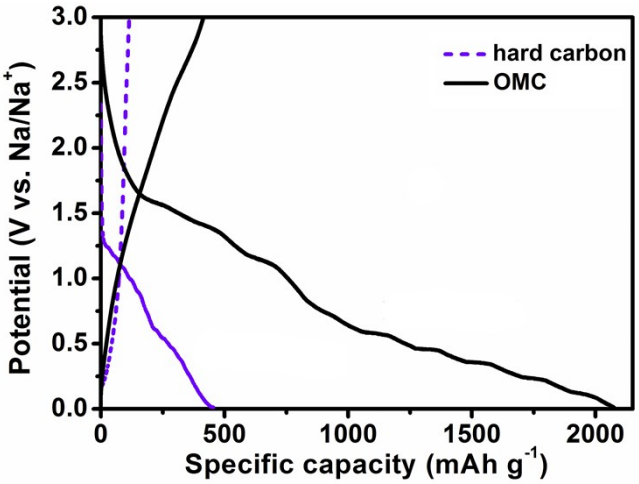

Fig.S6. GCD profiles for the first cycle of OMC and hard carbon at current density of 0.1 $A \cdot g^{-1}$.

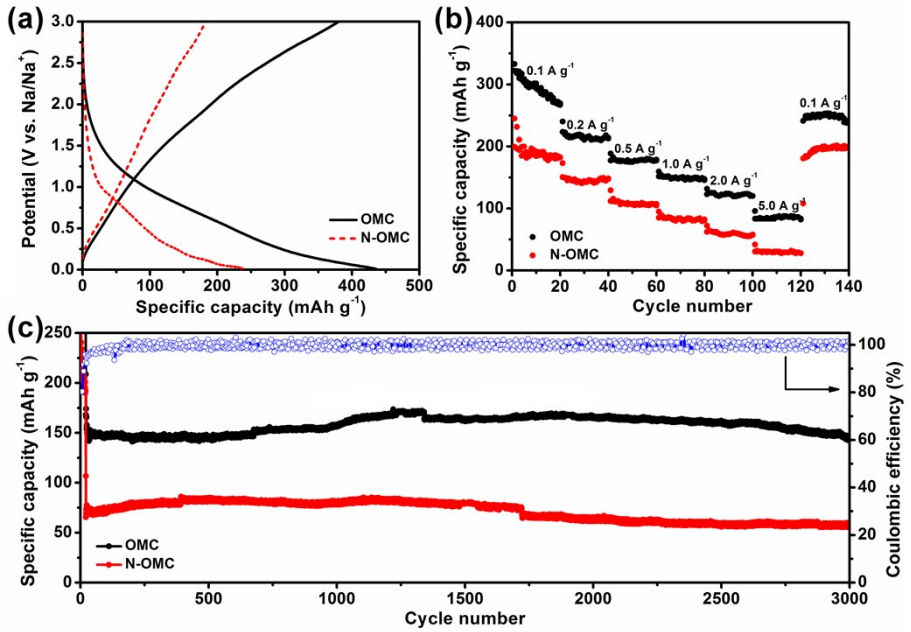

Fig.S7. (a) GCD profiles for the second cycle of OMC and N-OMC at current density of 0.1 $A \cdot g^{-1}$. (b) Rate capability of OMC and N-OMC. (c) Cycling stability of OMC and N-OMC at current density of 1.0 $A \cdot g^{-1}$.

The electrochemical properties of OMC and N-OMC as anode are tested and shown in Fig. S7. Although OMC and N-OMC have similar morphology and structure, the obviously different electrochemical properties can be observed. It should be noticed that the charge capacities for OMC and N-OMC are 380.2 and 183.1 $mAh \cdot g^{-1}$, respectively. The specific capacity of OMC is higher than that of N-OMC. And, the rate performance and cycling test also show same result that OMC is more suitable as anode material. By comparing the structure of OMC and N-OMC, we can guess that it may be due to the expanded interlayer spacing and higher graphitization degree for OMC. The detailed explanation will be made below.

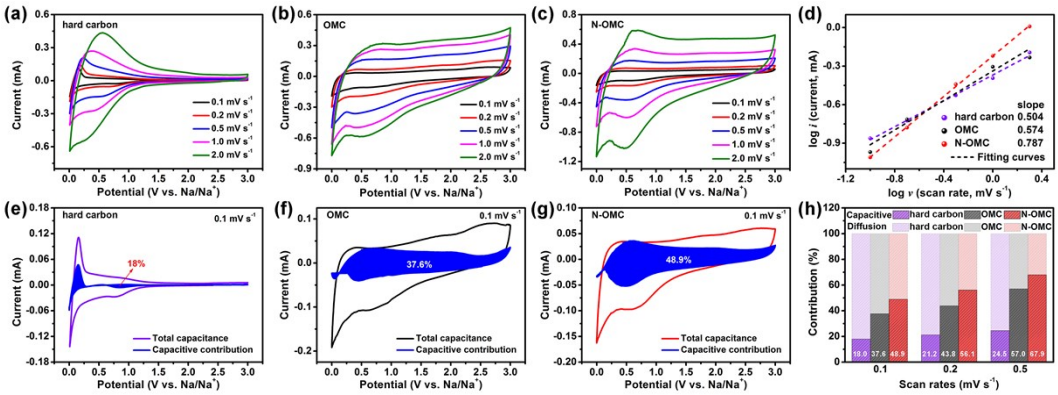

Fig.S8. CV curves of (a) hard carbon, (b) OMC and (c) N-OMC at different scan rates. (d) Determination of b value of hard carbon, OMC and N-OMC using the relationship between the peak current and the scan rate. The capacitive contribution of (e) hard carbon, (f) OMC and (g) N-OMC at scan rate of 0.1 mV·s^{-1}. (h) The contribution ratios of capacitive- and diffusion-controlled charge at different scan rates.

The b value of N-OMC as anode is obtained based on CV curves (Fig. S8c). The value is 0.787, which is bigger than the value of OMC (0.574), suggesting that the diffusion- and capacitive-controlled processes exist for N-OMC. According to the b-value results, N-OMC has faster reaction kinetics, but it provides lower capacity (Fig. S7) due to the lower proportion of faradaic reaction caused by less graphitic domain. It is necessary to ensure high capacity when improving the reaction kinetics. OMC is suitable as anode material of SIHCs. In addition, the capacitive contribution for N-OMC is calculated according to formula: $i(V) = k_1 v + k_2 v^{\frac{1}{2}}$, and the corresponding capacitive-controlled contribution to the total capacity is 48.9% at the scan rate of 0.1 mV·s^{-1}. The large capacitive contribution arises from high specific surface area and disordered carbon region that can provide numerous ions adsorption sites. Unfortunately, the low capacity

of N-OMC fails to meet the demand of SIHCs. From Fig. S8h, the capacitive contribution also increases along with increasing scan rates.

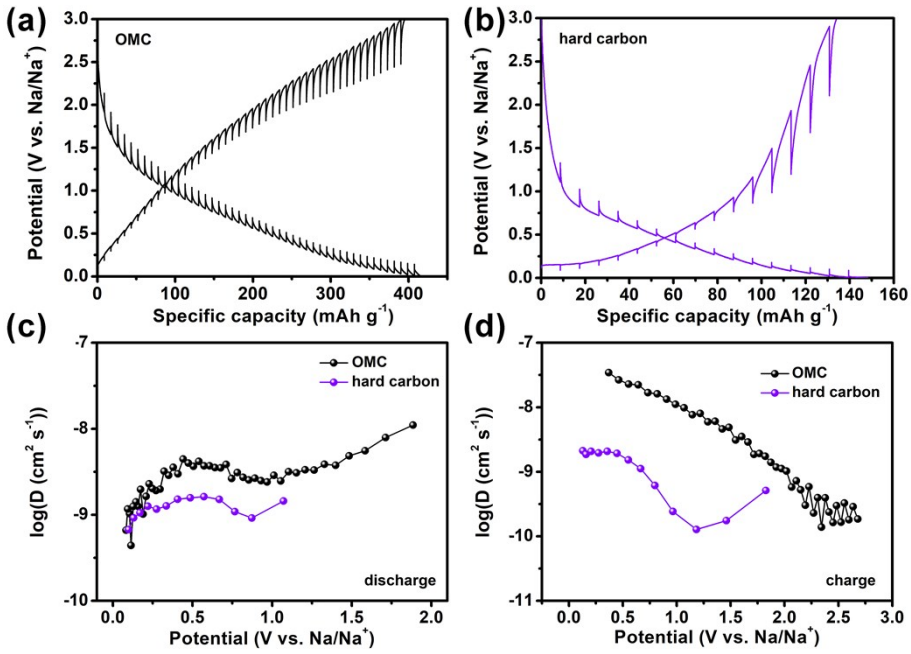

Fig.S9. GITT potential profiles of (a) OMC and (b) hard carbon. Na^+ diffusion coefficients at different potential during (c) discharge process and (d) charge process for OMC and hard carbon calculated from the GITT potential profiles.

To determine the reaction kinetics of OMC and hard carbon, the galvanostatic intermittent titration technique was used to assess the Na^+ diffusion coefficients according to the Fick's second law of diffusion. And the diffusion coefficient (D) can be calculated based on the following equation:[5]

$$D = \frac{4}{\pi\tau}\left(\frac{m_B V_m}{M_B S}\right)^2\left(\frac{\Delta E_s}{\Delta E_\tau}\right)^2$$

Where τ is the constant current pulse time (s), m_B is the mass of materials (g), V_m is the molar volume of materials ($cm^3 \cdot g^{-1}$), M_B is the molar mass of materials ($g \cdot mol^{-1}$), S is the geometric area of electrode materials (cm^2), ΔE_s is the voltage difference between the initial and steady state at single-step GITT test regardless of IR-drop, and ΔE_τ is the total voltage difference during the constant current discharge/charge process. The

M_B/V_m value corresponds to the density of material, and is calculated based on the following equation:[5]

$$\rho = \frac{1}{V_{total} + \frac{1}{\rho_{carbon}}}$$

Where ρ is the density of materials ($g \cdot cm^{-3}$), V_{total} is the total pore volume obtained by the N_2 adsorption-desorption isotherm of materials ($cm^3 \cdot g^{-1}$), and ρ_{carbon} is the true density of carbon ($g \cdot cm^{-3}$).

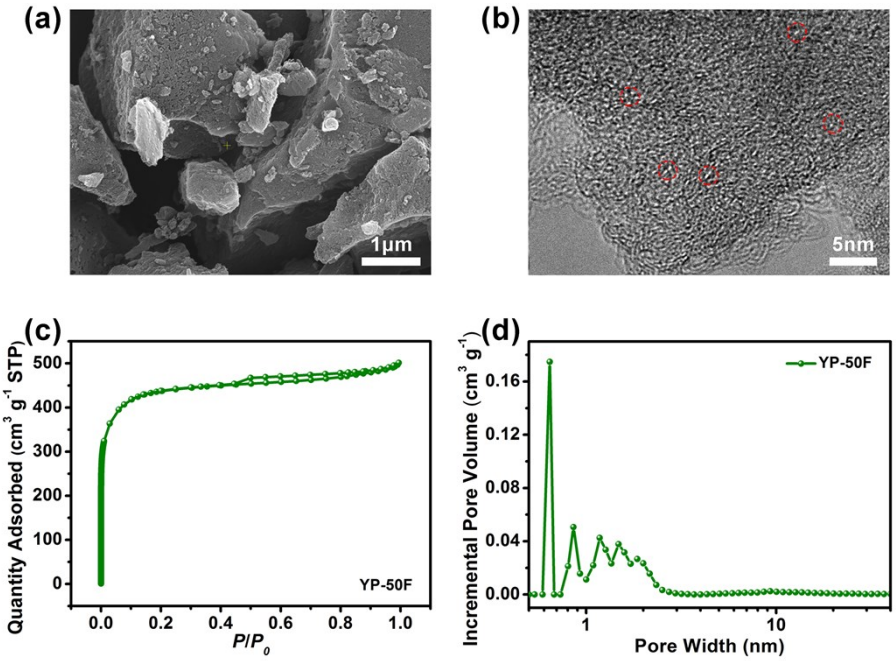

Fig.S10. (a) SEM and (b) HRTEM images of YP-50F. (c) N_2 adsorption-desorption isotherm and (d) Pore size distribution of YP-50F.

The morphology of commercial activated carbon (YP-50F) was characterized using SEM. We can observe that it is irregular, micron-sized block. The HRTEM image of YP-50F shown in Fig. S10b reveals that it is amorphous carbon and has numerous micropores identified by red circles. N_2 adsorption-desorption isotherm and pore size distribution of YP-50F are depicted in Fig. S10(c, d). The YP-50F can be ascribed to IUPAC type-I behavior, indicating microporous carbon structure. Brunauer-Emmett-Teller (BET) surface area is 1343 $m^2 \cdot g^{-1}$, and is dominated by pores between 0.6 and 2.3 nm. The pore structure parameters are listed in Table S1.

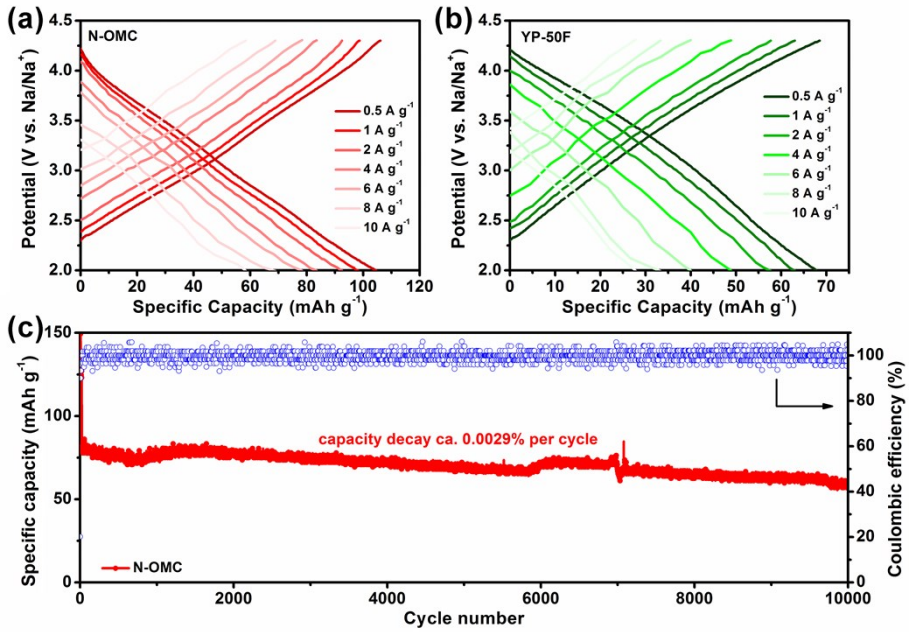

Fig.S11. GCD profiles of (a) N-OMC and (b) YP-50F at different current rates. (c) Cycling stability of N-OMC at current density of 5.0 $A \cdot g^{-1}$.

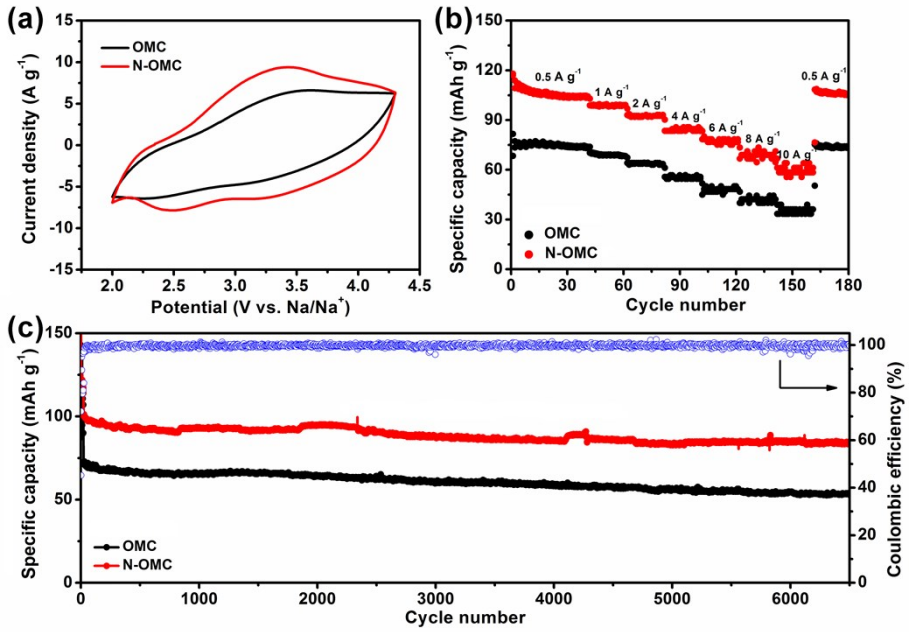

Fig.S12. (a) CV curves of OMC and N-OMC at scan rate of 40 $mV \cdot s^{-1}$. (b) Rate capability of OMC and N-OMC. (c) Cycling stability of OMC and N-OMC at current density of 1.0 $A \cdot g^{-1}$.

The CV curves of OMC and N-OMC at scan rate of 40 $mV \cdot s^{-1}$ are displayed in Fig. S12a, and the quasi-rectangular shape can be observed in the potential range of 2.0-4.3 V (vs. Na/Na^+). The CV area of N-OMC is higher than that of OMC, demonstrating higher charge storage for N-OMC. OMC and N-OMC have similar structure except for the nitrogen doping in N-OMC material, and it is reasonable to assume that the different in electrochemical property is most likely due to heteroatoms doping. In other words, introduction of heteroatoms greatly prompts the specific capacities. Furthermore, the more pronounced broad peaks can be observed on the CV curve of N-OMC, indicating the existence of pseudocapacitance ascribed to the nitrogen doping. The rate capability and cycling stability of OMC and N-OMC are shown in Fig. S12(b, c). The results

reveal that N-OMC has higher capacity. The rate capability and cycling stability for N-OMC are superior. Compared with OMC, N-OMC as cathode exhibits excellent electrochemical performance due to nitrogen doping.

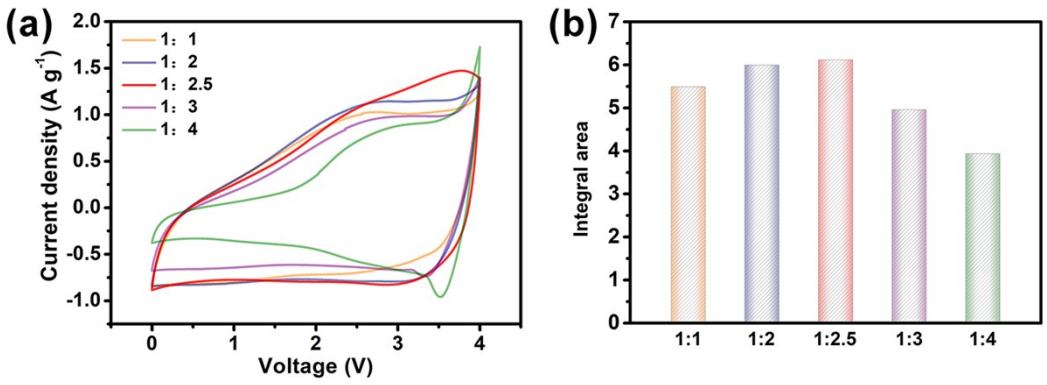

Fig.S13 (a) CV curves of OMC||N-OMC SIHC with different anode/cathode mass ratios at 20 $mV \cdot s^{-1}$. (b) The corresponding integral area of CV curves with different mass ratios (1:1, 1:2, 1:2.5, 1:3, 1:4).

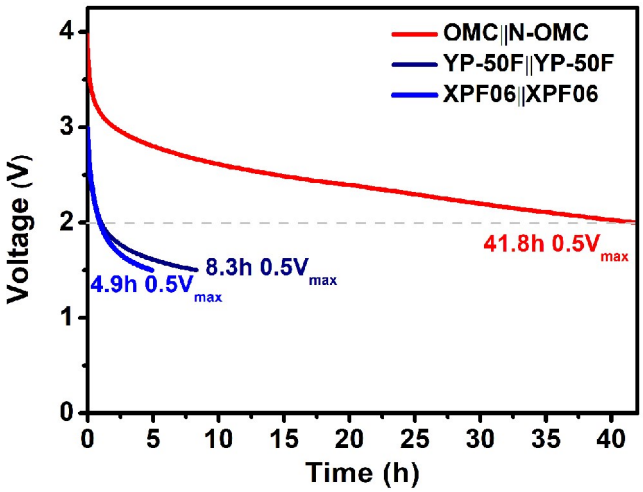

Fig.S14. Self-discharge curves of OMC||N-OMC in SIHC cell in comparison with electrochemical capacitors (XPF06||XPF06, YP-50F||YP-50F).

Table S1 Pore structure parameters of OMC and N-OMC

Sample	S_{BET} ($m^2 \cdot g^{-1}$)	V_{total} ($cm^3 \cdot g^{-1}$)	V_{micro} ($cm^3 \cdot g^{-1}$)
OMC	3421	1.750	0.97
N-OMC	2791	1.476	0.80
YP-50F	1343	0.775	0.52

Table S2 Chemical compositions of OMC and N-OMC from XPS

Sample	C (at%)	N (at%)	O (at%)
OMC	97.2	--	2.8
N-OMC	95.3	2.0	2.7

References

1. Z. X. Ma, T. Kyotani, Z. Liu, O. Terasaki and A. Tomita, *Chem. Mater.*, 2001, **13**, 4413.
2. Y. D. Xia, G. S. Walker, D. M. Grant and R. Mokaya, *J. Am. Chem. Soc.*, 2009, **131**, 16493.
3. X. C. Ren, Z. G. Ren, Q. W. Li, W. Wen, X. F. Li, Y. Chen, L. Xie, L. Zhang, D. M. Zhu, B. Gao, P. K. Chu and K. F. Huo, *Adv. Energy Mater.*, 2019, **9**, 1900091.
4. M. L. Kang, Y. Y. Wu, X. Huang, K. Q. Zhou, Z. G. Huang and Z. S. Hong, *J. Mater. Chem. A*, 2018, **6**, 22840.
5. X. Hu, G. B. Zhong, J. W. Li, Y. J. Liu, J. Yuan, J. X. Chen, H. B. Zhan and Z. H. Wen, *Energy Environ. Sci.*, 2020, **13**, 2431.